Gas transport properties through intact and fractured Callovo-Oxfordian mudstones

JON F. HARRINGTON[1]*, ROBERT J. CUSS[1] & JEAN TALANDIER[2]

[1]*British Geological Survey, Keyworth, Nottingham, UK*

[2]*Agence Nationale pour la Gestion des Déchets Radioactifs (Andra), 1/7, rue Jean Monnet, Parc de la Croix-Blanche, 92298 Châtenay-Malabry cedex, France*

**Correspondence: jfha@bgs.ac.uk*

Abstract: A series of controlled water and gas experiments was undertaken on samples of Callovo-Oxfordian (COx) mudstone using a synthetic fluid and helium gas. Data from this study demonstrate that the advective movement of gas through COx is accompanied by dilation of the original fabric (i.e. the formation of pressure-induced microfissures) at gas pressures significantly below that of the minimum principal stress. Flow occurs through a local network of unstable pathways, the properties of which vary temporally and spatially within the mudstone. The coupling of variables results in the development of significant time-dependent effects affecting many aspects of COx behaviour, from the gas breakthrough time to the control of deformation processes. Variations in gas entry, breakthrough and steady-state pressures may result from the arbitrary nature of the flow pathways and/or microstructural heterogeneity. Under these conditions, the data suggest that gas flow is along pressure-induced preferential pathways, where permeability is a dependent variable related to the number, width and aperture distributions of these features. This has important implications for modelling gas migration through low permeability, clay-rich materials.

In a repository for radioactive waste, hydrogen, carbon dioxide, nitrogen and hydrogen sulphide will be produced through a range of processes, including the corrosion of ferrous materials under anoxic conditions, the radioactive decay of the waste, the radiolysis of organic materials and water, and the microbial degradation of organic materials (Rodwell *et al*. 2003). Repositories for radioactive waste are designed and engineered (based essentially on ventilation and the specification of the waste) to limit high hydrogen concentrations and avoid explosive risks. In the French repository concept, hydrogen is the main gas that will be produced from the corrosion of metals. The production of hydrogen is anticipated to span in excess of 100 000 years post-emplacement of the waste, over which time the gas will move into the host rock through the combined processes of molecular diffusion and bulk advection. Understanding these processes and the long-term fate of the gas is therefore important in the development of a geological disposal facility for radioactive waste. In the French repository concept, the Callovo-Oxfordian (COx) Formation, which is classed as an indurated mudstone for the purposes of this paper – although the actual clay content varies depending on its location in the geological sequence, as illustrated in Robinet *et al.* (2015) – has been proposed as a candidate host rock for the long-term disposal of the nation's radioactive waste. As such, much attention has focused on the Paris Basin, where COx occurs as a thick unit (*c.* 130 m) of uninterrupted mudstones. Based on initial surface measurements and from the direct observation of experiments housed in the Meuse/Haute Marne Underground Research Laboratory constructed at Bure, NE France, the site appears to offer very favourable conditions for the siting of a repository, including a low hydraulic conductivity (Harrington *et al.* 2012*a*; Cuss *et al.* 2014), small molecular diffusion rates, a significant retention capacity for radionuclides (Altmann *et al.* 2012) and minimal seismic activity (Cara *et al.* 2015).

However, these properties, in particular the low permeability of the host rock, can severely restrict the movement of gas, which can thus accumulate (Wikramaratna *et al.* 1993; Ortiz *et al.* 2002; Weetjens & Sillen 2006) until the pressure becomes large enough to cause the gas to enter the surrounding host rock (Harrington & Horseman 1999). Recent studies (Horseman *et al.* 1996, 2004; Harrington & Horseman 1999; Angeli *et al.* 2009; Harrington *et al.* 2009, 2013, 2014; Cuss *et al.* 2014) suggest that in the case of clay-based materials and, in particular bentonite, the gas flows through a series of pressure-induced pathways that open and close to allow its passage through the system.

From: Rutter, E. H., Mecklenburgh, J. & Taylor, K. G. (eds) 2017. *Geomechanical and Petrophysical Properties of Mudrocks*. Geological Society, London, Special Publications, **454**, 131–154.
First published online April 3, 2017, https://doi.org/10.1144/SP454.7

To further understand the key processes governing water and gas flow through the COx, the French radioactive waste management company, Agence Nationale pour la Gestion des Déchets Radioactifs (Andra) and the British Geological Survey undertook a series of laboratory-scale tests on preserved COx rock samples. Data from that study are presented here to illustrate the specific behaviour regarding the key phenomenological processes operating in the COx during water and gas flow. Detailed explanations of the individual tests described in this paper can found in Harrington *et al.* (2014) (samples COx-1 and COx-2) and Cuss *et al.* (2012) (samples SPP_COx-1 and SPP_COx-2). This paper summarizes the salient observations related to hydraulic properties and gas flow at key stages, including consolidation, hydraulic flow, gas entry and breakthrough, and steady-state gas flow, and shut-in, self-sealing and fracture flow behaviours. This paper represents the current state of our scientific knowledge of advective flow behaviour, combining previous measurements with new results from detailed laboratory tests and thereby identifying gaps in our current understanding.

Basic theory

The equation of porewater flow is obtained by combining Darcy's law with the equation of fluid mass conservation to give (de Marsily 1986):

$$\frac{S_s}{\rho_w g}\frac{\partial p_w}{\partial t} = \nabla . \left(\frac{k_i}{\mu_w}(\nabla p_w + \rho_w g \nabla z)\right) + Q \quad (1)$$

where S_s is the specific storage (m^{-1}), k_i is the intrinsic permeability (m^2), ρ_w is the density of water (kg m^{-3}), g is the acceleration due to gravity (m s^{-2}), μ_w is the viscosity of water (Pa s), p_w is the porewater pressure (Pa), z is the vertical coordinate (m) and Q is the rate of fluid volume injection per unit volume of porous medium (s^{-1}). This equation is solved here by the finite element method for an axisymmetric two-dimensional domain subject to specified head and specified flow boundary conditions. Hydraulic head, h (m), is related to the porewater pressure by $p_w = \rho_w g(h - z)$.

To model consolidation test data, it is necessary to couple the porewater flow equation with equations for the stress–strain relationships. The porewater equation for this takes the form given by Huyakorn and Pinder (1983):

$$\nabla . \left(\frac{k_i}{\mu_w}(\nabla p_w + \rho_w g \nabla z)\right) = \varphi\beta\frac{\partial p_w}{\partial t} + \frac{\partial}{\partial t}(\nabla . u) \quad (2)$$

where ϕ is the porosity, β is the fluid compressibility (Pa^{-1}) and u is the vector of solid phase displacements (m). For the case of elastic plane strain, the equations for the displacements are:

$$\frac{E}{2(1+\nu)}\nabla^2 u + \frac{E}{2(1+\nu)(1-2\nu)}\nabla(\nabla \cdot u) - \nabla p_w = 0 \quad (3)$$

Here E is Young's modulus (Pa) and ν is Poisson's ratio. Equations (2) and (3) are solved using the finite element code STAFAN (INTERA 1983), fitting E and k_i to the asymptote and transient of the cumulative outflow curve, respectively, measured during consolidation. Parameters derived in this way represent bulk values with no directional component.

In the case for the steady-state flow of gas as a single phase in a porous medium, the equation may be rewritten by combining the mass continuity equation with a generalization of Darcy's law:

$$\nabla . \left(\frac{\rho_g k_g}{\mu_g}\nabla(p_g)\right) = 0 \quad (4)$$

where p_g is the gas pressure (Pa), ρ_g is the gas density (kg m^{-3}), k_g is the effective gas permeability (m^2) given by $k_g = k_{rg}k_i$, where k_{rg} is the relative permeability to gas, and μ_g is the gas viscosity (Pa s). Assuming ideal gas behaviour and a constant value for k_g, equation (4) can be integrated along a one-dimensional flow path to obtain an expression for the flow rate at STP, Q_{st}, in terms of the pressures at either end of the path:

$$Q_{st} = \frac{\nu_{mst} k_g A}{2RT\mu_g L}(p_{gi}^2 - p_{go}^2) \quad (5)$$

where ν_{mst} is the molar volume of the gas at STP, A is the specimen's cross-sectional area (m^2), L is the specimen's length (m), R is the gas constant, T is the absolute temperature (K), p_{gi} is the gas pressure at injection (Pa) and p_{go} is the pressure at outlet (Pa). Although gas pressure p_{go} cannot be measured directly in these experiments, it can be related to the back-pressure of the water at the downstream end of the specimen, p_{wo}, by the relationship $p_{go} = p_{wo} + p_{co}$, where p_{co} is the apparent capillary threshold pressure.

Experimental systems and procedures

The basic permeameter consists of five main components: (1) a specimen assembly; (2) a 70 MPa rated pressure vessel and associated confining

pressure system; (3) a fluid injection system; (4) a back-pressure system; and (5) a PC-based data acquisition system. Specimens are subjected to a confining stress, with the injection platen located on the base of the specimen. A novel feature of the apparatus is the use of porous annular guard-ring filters around the inflow and outflow filters (Fig. 1a). The pressures in these two guard-rings can be independently monitored and can be used to provide additional information, such as pore pressure evolution, hydraulic anisotropy and flow symmetry.

Volumetric flow rates are controlled or monitored using a pair of high-precision syringe pumps operated from a single digital control unit. Movement of the pump piston is controlled by a microprocessor, which continuously monitors and adjusts the rate of rotation of an optically encoded disc (graduated in segments equivalent to a change in volume of >31.71 nl) using a DC motor connected to the piston assembly via a geared worm drive. This allows each pump to operate in either constant pressure or constant flow modes. A program written in LabVIEW elicits data from the pump at pre-set time intervals. Testing was performed in an air-conditioned laboratory at a nominal temperature of 20°C to minimize thermal noise in the data. All pressure transducers were calibrated against a known laboratory standard and corrections were applied to the presented data, yielding coefficients of determination (r^2) >0.999.

Two variants of the apparatus were used (Fig. 1a). In the first, an isotropic confining stress was applied to the sample with the data on volume change derived by careful measurement of the confining reservoir volume; see Harrington *et al.* (2013) for a full description of the apparatus. In the second triaxial system, the axial and radial stress were controlled independently with the strain continuously monitored (both axially and radially), providing real-time data on the volume change of the sample; see Cuss *et al.* (2014) for a full description of the apparatus. Radial strain was measured orthogonally with sub-micron precision by three 'dash-pots' that contacted the outside of the specimen jacket directly at the mid-plane of the sample.

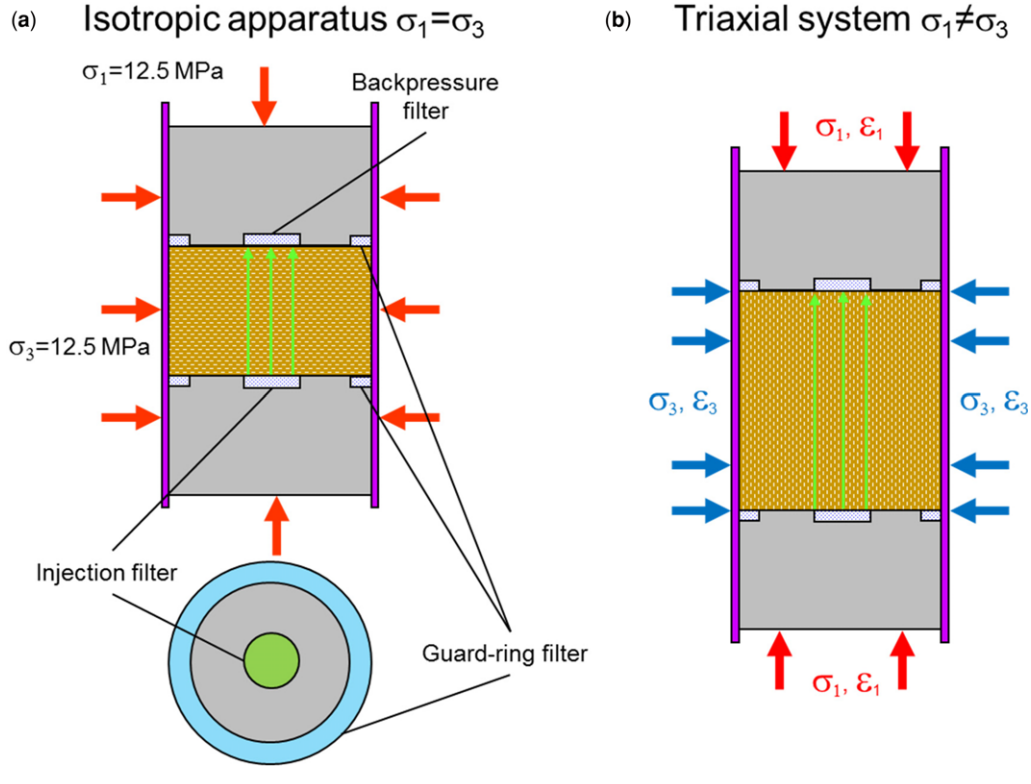

Fig. 1. Schematic diagram showing (**a**) isotropic and (**b**) triaxial test systems. The flow in and out of the sample was controlled by high-precision syringe pumps. Each geometry was used to define the swelling/consolidation and hydraulic and gas migration properties. The sample in the triaxial system was mounted horizontally.

A small differential stress of 1.0 MPa was maintained between the axial and radial stresses throughout each experiment to prevent the sample going into extension.

To minimize the chance of slug flow during gas testing, both permeants (gas and water) were injected at the base of the specimen for the isotropic system and from one end of the sample for the triaxial system, the latter being mounted horizontally. To limit osmotic swelling of the specimen, a synthetic porewater solution was prepared for use as the back-pressurizing fluid and permeant during the hydraulic test stages. Details of the hydrochemistry of the interstitial fluid were provided by Andra (Gaucher *et al.* 2007). During gas testing, helium was selected as a safe substitute for hydrogen to measure the gas transport properties of the mudstone. *In situ* (isotropic) confining stress data were provided by Andra and an initial confining stress of 12.5 MPa and a back-pressure of 4.5 MPa were selected.

Four test plugs were prepared for isotropic testing. The first two, designated COx-1 and COx-2, were oriented with the plugs' cylindrical axis perpendicular to the bedding, whereas the third, COx-3, was oriented parallel to the bedding. The fourth plug, designated COx-4, was initially prepared perpendicular to bedding, but contained a natural fracture spanning the full length of the core. However, the discontinuity retained some degree of cohesion between the fractured segments and remained 'intact' during preparation (Fig. 2). In addition to these samples, two specimens designated SPP_COx-1 and -2 were prepared for use in the triaxial system using the outlined methodology. Specimen SPP_COx-1 was subject to a detailed hydromechanical stress path to define the point of failure and has been reported previously by Cuss & Harrington (2010, 2011); test SPP_COx-2 was used to measure the hydraulic and gas transport properties of the COx (Cuss & Harrington 2012).

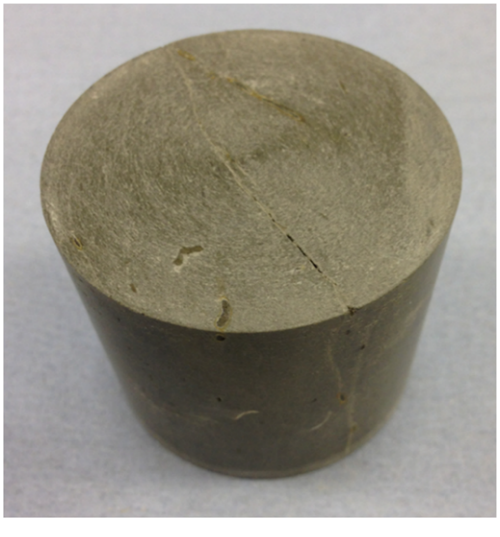

Fig. 2. Photograph showing natural fracture through sample COx-4.

Following initial re-saturation of the samples, each test consisted of a sequence of test stages. A consolidation stage involved incrementally increasing the confining pressure and measuring the volume of fluid displaced while the back-pressure (and injection pressure) were held constant. Constant pressure hydraulic and gas stages were used to evaluate the intrinsic permeability, specific storage, gas entry and breakthrough pressure, apparent threshold capillary pressure and gas permeability. At the end of hydraulic testing, a pressure recovery stage allowed excess porewater pressures to dissipate.

Geotechnical data

Field sampling and subsequent transportation of the core were undertaken with care to minimize damage and desiccation. Cores were drilled perpendicular and parallel to bedding from the underground laboratory at Bure and shipped in specially designed core holders, designated T-cells, in which the preserved core was subjected to an axial load imposed by a strong retaining spring. Upon receipt of the T-cells in the laboratory, the material was catalogued and stored under refrigerated conditions at 4°C to minimize biological and chemical degradation. Test specimens were prepared by sub-sampling the field material using a combination of dry core drilling (with gas flushing and the vacuum removal of fines), diamond slicing, surface grinding and machine lathing. The curved surfaces of the specimen were covered with a thin coat of high-purity silicone sealant to provide an effective seal between the Teflon sheath and the rock surface. Off-cuts from the coring process were weighed and oven-dried to obtain an estimate of moisture content. The dimensions, orientation and provisional geotechnical properties of the specimen are given in Table 1.

Consolidation data

To understand the consolidation behaviour of COx, samples COx-1 to COx-3 were subject to a multi-step consolidation test prior to hydraulic/gas testing (Harrington *et al.* 2012*a*). The tests consisted of an initial equilibration period, with the confining pressure at 9.5 MPa and the porewater pressure at 4.5 MPa, followed by two steps up in confining pressure to 11 MPa and then 12.5 MPa for samples

Table 1. *Basic physical properties of specimens prior to testing*

Specimen	Orientation to bedding	Length (mm)	Diameter (mm)	Moisture content (%)	Bulk density (Mg m^{-3})	Dry density (Mg m^{-3})	Porosity (%)	Saturation (%)
COx-1	Perpendicular	53.9	54.4	6.1	2.45	2.31	14.6	97
COx-2	Perpendicular	55.0	54.4					
COx-3	Parallel	63.7	54.5	6.2	2.45	2.31	14.6	98
COx-4	Perpendicular	63.7	54.5					
SPP_COx-1	Parallel	76.6	55.5	5.7	2.46	2.33	14.2	93
SPP_COx-2	Parallel	82.5	55.9	6.2	2.45	2.31	14.8	96

An assumed specific gravity for the mineral phases of 2.70 Mg m^3 (Zhang *et al.* 2007) was used in these calculations. Data for COx-2 not available as test is ongoing. Data for COx-4 is unavailable as the sample was sub-sectioned directly after testing for further analysis. Values for COx-3 based on estimated dry weight derived from SPP_COx-2, which came from the same core barrel.

COx-1 and COx-2 and to 11.5 and 12.6 MPa for sample COx-3. The instantaneous flow rate and net cumulative flow volume data were collected, with the latter equating to volumetric strain. The data show well-defined transient responses in the back-pressure system for each increment in confining stress.

An analysis of the consolidation data, based on the total volume of fluid expelled from the specimen at the end of each step, is presented in Table 2. This analysis assumed an isotropic medium with parameters derived from the change in volume of the sample for a change in confining stress. Values for the drained bulk modulus obtained in this way are reasonably high, ranging from 1490 to 2262 MPa. These values suggest that the specimen has not been subject to significant damage from de-stressing during sampling, transportation or specimen preparation. Young's modulus values ranged from 1764 to 2629 MPa. These values are lower than those quoted by Gens *et al.* (2007), who suggested values in the range 4000–5600 MPa. However, a significant component of the difference probably relates to the mode of measurement. The values presented in this study were derived from the amount of cumulative water displaced (reflecting the pore compressibility of the mudstone, β_p), whereas many quoted values are derived from the direct measurement of strain (including mineral and pore compressibility terms). Although both methods of measurement are valid, care should be taken in the selection of parameters, which should reflect the specific problem under investigation.

Additional analysis of the consolidation tests was undertaken using a finite element coupled deformation and porewater flow model of the experimental configuration. For these calculations, the anisotropy of the permeability obtained from the

Table 2. *Summary of results from consolidation tests*

Stage no.	Average effective stress (MPa)	Void ratio (at end of stage)	Volumetric strain (%)	Drained compressibility $\beta_p/10^{10}$ (Pa^{-1})	Drained bulk modulus (MPa)	Young's modulus (MPa)
Data for COx-1						
1	5.0	0.175				
2	6.5	0.174	0.07	4.4	2262	2629
3	8.0	0.173	0.16	6.4	1574	1870
Data for COx-2*						
1	5.0					
2	6.5		0.09	5.6	1759	2092
3	8.0		0.19	6.7	1490	1764
Data for COx-3†						
1	5.0	0.171				
2	7.0	0.170	0.11	5.3	1902	2340
3	8.1	0.169	0.16	4.7	2133	2381

Values for Young's modulus are based on a Poisson's ratio of 0.3 (Wileveau & Bernier 2008).
*Void ratio data is not available as test is ongoing.
†Values based on estimated dry weight derived from SS_COx-2, which came from the same core barrel.

Table 3. *Summary of results of finite element modelling of consolidation tests*

Sample	Stage	K_h (m^2)	k_z (m^2)	E (MPa)	S_s (m^{-1})
COx-1	2	10.6×10^{-21}	4.0×10^{-21}	1825	7.2×10^{-6}
	3	9.0×10^{-21}	3.4×10^{-21}	1700	7.7×10^{-6}
COx-2	2	6.6×10^{-21}	2.5×10^{-21}	1600	8.1×10^{-6}
	3	6.6×10^{-21}	2.5×10^{-21}	1450	8.9×10^{-6}

hydraulic tests (taken as 2.65) was used for each sample and a value of 0.3 was assumed for Poisson's ratio (Wileveau & Bernier 2008). Then, for each sample, the value of Young's modulus was adjusted to fit the magnitude of the net flow volume in each step while the permeability was adjusted to fit the transients. Because the code handles only two-dimensional and axisymmetric configurations, the test for sample COx-3 could not be analysed in this way because of the parallel to bedding orientation of the sample. Table 3 shows the results of these calculations.

Hydraulic behaviour

Following the consolidation tests, each isotropic and triaxial sample was subjected to a constant pressure hydraulic test, while the back-pressure and confining pressure were held constant. In each case, the back-pressure was held at 4.5 MPa while the injection pressure was stepped up to 7.5 MPa and then back down to 4.5 MPa. The data from these tests were fitted using a finite element porewater flow model and the results are presented in Table 4. However, pressure data from the injection and back-pressure guard-rings were not used to calculate the hydraulic anisotropy on this occasion as a result of concerns relating to bypass flow across the platen face from the guard-ring to the central filter. As such, data from the guard-rings were used to estimate the anisotropy of the formation and only the estimated value for the axial component of the permeability is reported. This is in contrast with the data presented in Harrington *et al.* (2012*a*), which should be treated with some caution. In this way, a more realistic estimate of hydraulic anisotropy may be obtained from the average of the axial permeabilities from samples COx-1 and COx-2 for permeability perpendicular to the bedding and from sample COx-3 for permeability in the plane of the bedding. This gives an anisotropy of 2.5.

Gas transport through intact COx

Gas entry and breakthrough

Analysis of the data from isotropic and triaxial experiments (Harrington *et al.* 2014; Cuss *et al.* 2014) found that the gas entry pressures exhibited a degree of variability ranging from *c.* 1.0 MPa for test COx-1 to >5 MPa in test COx-2. The analysis of small precursor flows, observed in a number of tests prior to gas entry and subsequent breakthrough, indicated that these were aqueous in origin and were predominantly derived from water displaced from injection and the guard-ring filters. Post-test analyses of sample saturation found no evidence of the displacement of water from the original porosity of the mudstone.

Figure 3 shows a compilation of gas breakthrough data for the COx plotted against sample thickness derived from measurements by different researchers. Inspection of the data suggests domains of behaviour, with the shorter samples, which are prone to damage (during initial sampling and sample manufacture), yielding generally lower breakthrough pressures. The application of a high confining stress to shorter samples appears to aide pathway closure, suggesting both possible damage and localization of the gas flow. However, this evidence is circumstantial and further work is required to understand the role of local heterogeneities within

Table 4. *Summary of results from hydraulic tests*

Sample	k_z (m^2)	K_h (m^2)	S_s (m^{-1})
COx-1	1.8×10^{-21}		5.4×10^{-6}
COx-2	1.6×10^{-21}		6.0×10^{-6}
COx-3		4.5×10^{-21}	6.0×10^{-6}
COx_SPP-2		$5.8–7.0 \times 10^{-21}$	13.0×10^{-6}

COx-1 and COx-2 were oriented perpendicular to bedding, while COx-3 and COx_SPP-2 were parallel to bedding.

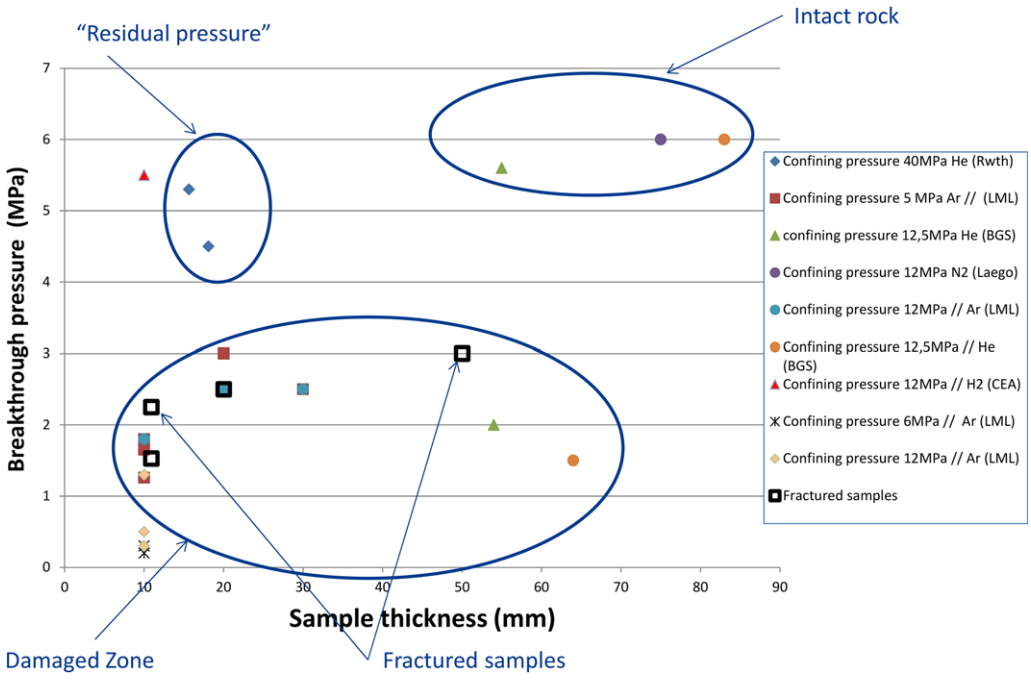

Fig. 3. Compilation of gas breakthrough data plotted against sample length. LML, Song *et al.* (2016); Mjahad (2012); BGS-Laego, Cuss *et al.* (2014); CEA, Didier (2012); RWTH, Krooss & Alles (2008). The data suggest domains of behaviour related to induced and or natural heterogeneities within the mudstone.

the samples. At present, such features are likely to bias data from shorter samples, leading to apparently low gas breakthrough pressures. It is entirely possible that the *in situ* gas breakthrough pressure of COx is >5 MPa, as observed by Cuss & Harrington (2012).

Inspection of the experimental data indicates that the process of gas breakthrough is associated with the time-dependent development of a network of conductive pathways (Fig. 4). These localized features appear to evolve over days, weeks or even months before the system attains a true steady state, even across the relatively short flowing distances associated with laboratory specimens. As an example of this phenomenon, data from test COx-2 are shown in Figure 4a, which shows the gradual and complex evolution in flow and guard-ring pressures as gas begins to propagate across the sample. The entire process from entry to final steady state takes >200 days and is indicative of pathway dilatancy/drainage rather than a classic macro-scale fracturing process.

Further evidence of the processes involved during gas breakthrough can be seen in Figure 4b from triaxial test SPP_COx-2. Here the development of flow is clearly associated with the change in bulk volume of the sample, which radially dilates to accommodate the passage of gas across the sample. The amount of strain appears non-uniform, providing additional evidence for the localization of gas flow within the mudstone. As in Figure 4a, the evolution in flow and strain occurs over a significant period of time. The relationship between gas pressure, total stress, volumetric strain and their coupling to the number and distribution functions of gas-induced pathways remains unclear. However, the necessity for the mudstone to undergo a change in volume to develop advective gas permeability may account for the observed time-dependent effects.

Steady-state flow and gas permeability

A number of flow tests were undertaken to specifically examine the apparent 'drainage-imbibition' response of the mudstone to define the relationship between gas pressure gradient, flow rate, saturation and permeability. In test COx-1, the injection pressure was gradually increased in seven steps to define the initial 'drainage' behaviour. This was followed by two decreases in pressure to define the hysteretic response during 'imbibition'. Figure 5a shows the flux and injection pressure data for test COx-1. Inspection of the graph shows a number of clear

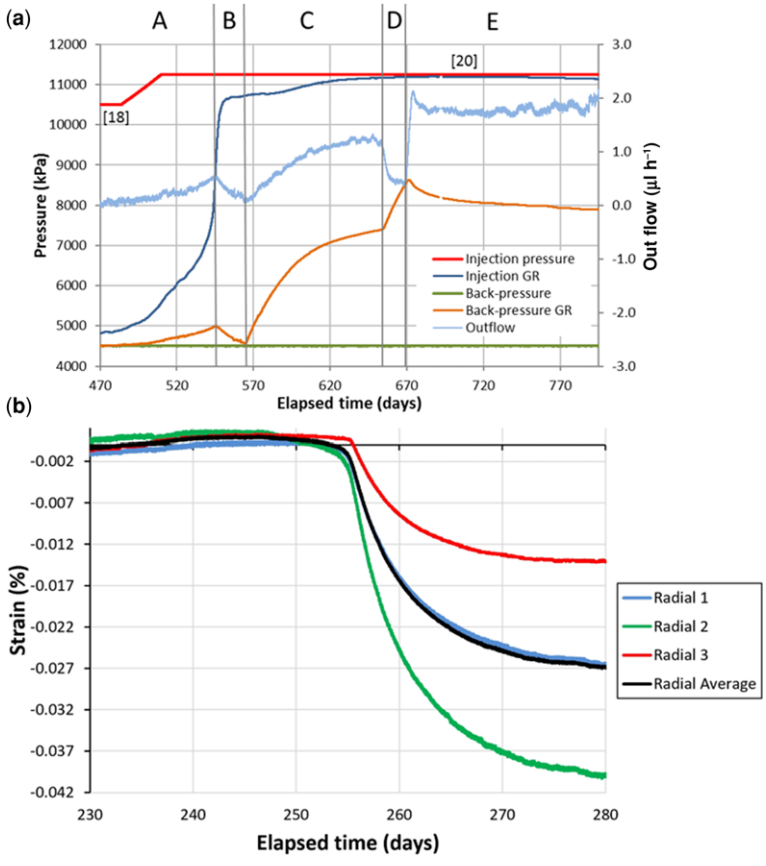

Fig. 4. (**a**) Sample COx-2: material response during gas entry and subsequent breakthrough (GR, guard-ring). Zone index: A, dewatering of IGR filter; A–B, migration of gas across the sample; C, outflow dominated by drainage of water BGR filter; D, as BGR filter is drained of water, the gas pressure increases; and E, gas breakthrough occurs. (**b**) Outflow and strain data during gas entry and subsequent breakthrough for sample SPP_COx-2. Data show dilatant response of sample in the development of advective gas permeability.

events: major gas breakthrough, stage 9, occurs after a significant period of time; the evolution of gas flow significantly lags behind the change in gas pressure gradient resulting in protracted flow transients; variations in outflow, stages 11 and 15, suggest unstable pathway flow; and hysteresis is observed between the 'drainage' and 'imbibition' cycles. This latter point is evident in Figure 5b, which clearly shows the hysteresis between ascending and descending flow cycles. The underlying cause for this hysteresis remains unclear, but may relate to time-dependent stress–strain processes associated with changes in pathway aperture. However, Figure 5b indicates that, as the gas pressure decreases, a residual network of conductive pathways appears to remain within the mudstone, stage 21. The longevity of these features will be discussed in the following section on shut-in and self-sealing behaviour.

Considerable data now exist indicating that the pathways formed during the advective movement of gas are both dynamic and unstable, opening and closing in response to local changes in gas pressure and its hydromechanical coupling with the fabric of the mudstone (as reviewed in Harrington *et al.* 2014). These changes can be both rapid, signified by spontaneous changes in the guard-ring pressure and flow (Fig. 6a), or relatively slow, indicated by the protracted flow transients observed following a change in gas pressure gradient (Fig. 5a).

Close inspection of the data indicates that the dynamic pathway behaviour continues even at steady state and can result in the slow, progressive erosion of gas permeability, leading to a zero flow condition. This spontaneous loss of gas permeability was observed in triaxial test SPP_COx-2 (Fig. 6b). Here the relationship between the creation of

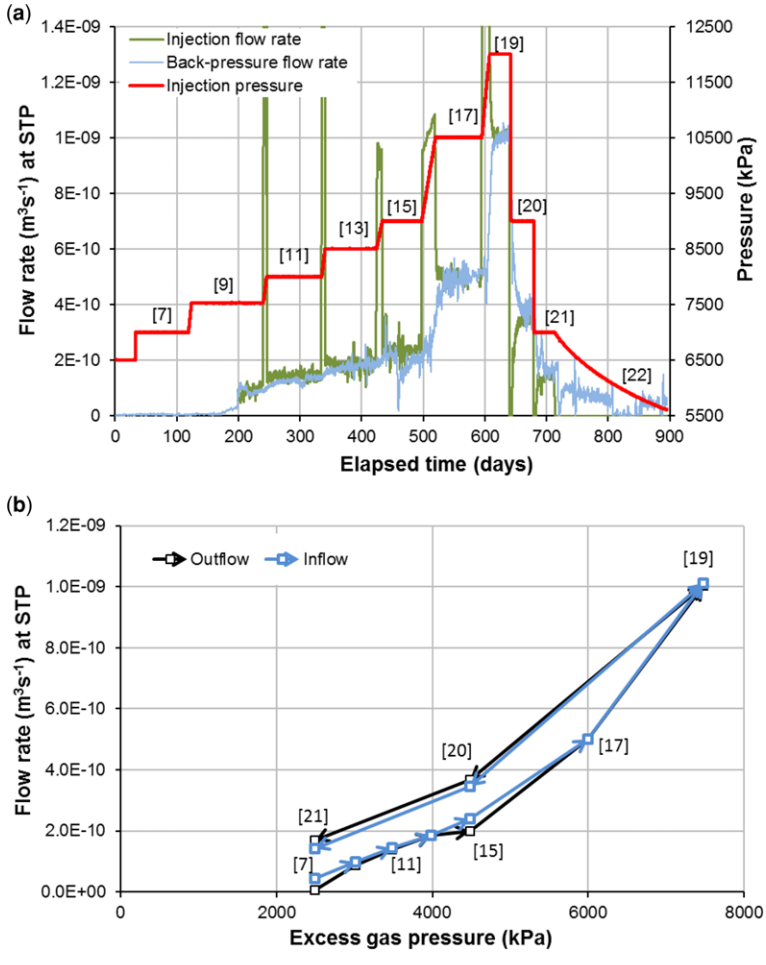

Fig. 5. (**a**) Gas flow rates at the injection and back-pressure filters during gas injection test COx-1. The large spikes in injection flux relate to the compression of the gas phase during constant flow rate test stages. (**b**) Cross-plot of flow in and out the sample plotted against excess gas pressure. The hysteresis between ascending and descending flow cycles is evident in the data.

gas permeability, signified by the development of outflow, and the change in bulk volume of the sample, is clearly evident. However, at day 320 the outflow spontaneously decreased for no apparent reason, resulting in a reduction in permeability and a protracted strain transient, the end-point of which suggests that trapped gas within the sample may have temporally altered the volumetric hysteresis of the sample. Such behaviour may be symptomatic of the movement of gas along a relatively small number of unstable dilatant pathways, an observation supported by post-test saturations that show no measureable desaturation. This instability in the number of conductive gas pathways and the subsequent loss of permeability may be linked to time-dependent changes in the fabric of the structure.

The coupling between volume change and gas flow was explored in a number of tests, in particular COx-3, which examined the relationship between the steady-state flow rate, the gas and porewater pressure and its coupling to volumetric strain (the latter derived from changes in confining system volume). In this test, consecutive increments in the gas pressure gradient of 3 and 1 MPa were systematically applied to the sample by increasing either the injection or back-pressure values (Fig. 7a). This was followed by decreases in pressure, remapping the original ‘drainage’ curve. An initial analysis of the data (Fig. 7b) appears to show no obvious trend

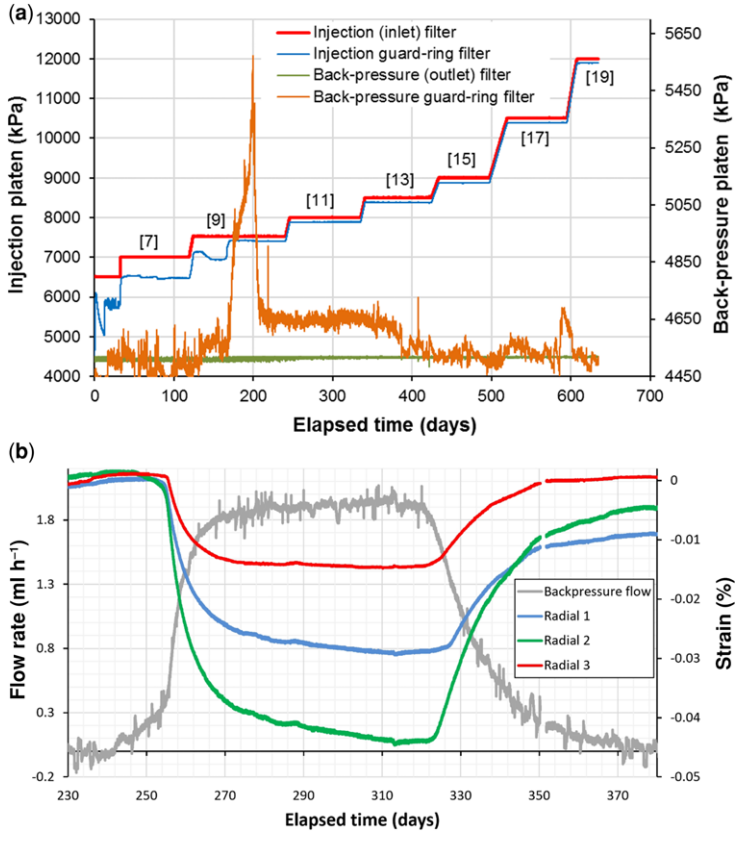

Fig. 6. (**a**) Pressure from the injection, back-pressure, and guard-ring filters during the initial drainage phase of test COx-1. (**b**) Outflow and strain data from triaxial test SPP_COx-2 showing the coupling between the creation of conductive gas pathways and the bulk volume change of the sample (-ve strain = volume expansion).

linking the steady-state flow rate to the average effective stress, σ_{eff}, defined for the purposes of this paper as:

$$\sigma_{\text{eff}} = \sigma - \frac{(p_{\text{gi}} + p_{\text{wo}})}{2} \tag{6}$$

where σ is the total stress (Pa), p_{gi} is the pressure of gas in the injection system and p_{wo} is the external water pressure. In reality, the p_{wo} term should be replaced by p_{go}, reflecting the elevated gas pressures inside the sample at the downstream end of the core. Although no p_{co} value was available, its inclusion would have no effect on the relationships observed, but would simply shift the data left in the stress space in Figure 7.

However, when the volumetric strain was substituted for the flow rate (Fig. 7c), a clear trend emerged where the volume change was an integral component in the development of flow and therefore gas permeability. Although this method of volumetric strain determination is rather crude, it appears that much, if not all, of the strain is recovered during the course of the test. This observation corresponds well with the data derived from the more detailed triaxial testing (Fig. 5b).

In contrast with the hysteresis data presented in Figure 5b, flux across the sample reduced slightly after stage 16, which suggests that the magnitude of the volumetric flow rate across the sample was also dependent on the absolute values of the gas and porewater pressure, rather than simply the difference between the two. This potential history and pressure dependence of gas flow in COx is not understood and remains absent from current modelling approaches.

The importance of the absolute values of gas and water pressure emerges still further in Figure 7d, which shows a cross-plot of gas permeability against average effective stress. The incremental/decremental changes in porewater pressure, in order to

reduce the gas pressure gradient to 1.0 MPa, have a far stronger influence on the apparent permeability than when the injection gas pressure alone is simply increased/decreased. This suggests that the reduction in average effective stress that accompanies the reduction in gas pressure gradient from 3.0 to 1.0 MPa has an important effect on absolute permeability and that the reduction in effective stress may actually enhance pathway dilatancy.

The general response of sample COx-2 is in contrast with the data from triaxial test SPP_COx-2 and the repeat gas breakthrough pressure of test COx-2. As such, further work on hydromechanical–gas permeability coupling is required to better understand the typical response of COx to the migration of gas.

Shut-in and self-sealing behaviour

To estimate the apparent capillary threshold value (i.e. the point at which gas ceases to be mobile within the clay), the injection pump was switched off in test COx-1, stage 22 (Fig. 5a) and the excess gas pressure was allowed to decay. Figure 8a shows the slow time-dependent decrease in pressure as the permeability within the sample deceases (this is similar in form to the change in outflow noted in Fig. 6b as flow spontaneously decreases). The length of the transient is a direct consequence of the non-linearity in the gas flow law. However, an estimate of the transient length can be obtained using the governing differential equation for axial flow (Harrington & Horseman 1999):

$$V_{\mathrm{gi}}\frac{\mathrm{d}p_{\mathrm{gi}}}{\mathrm{d}t}+\ p_{\mathrm{gi}}\frac{\mathrm{d}V_{\mathrm{gi}}}{\mathrm{d}t}=B(p_{\mathrm{go}}^2-p_{\mathrm{gi}}^2) \qquad (7)$$

where p_{gi} and V_{gi} are the pressure and volume of gas in the injection system, p_{go} is the sum of the external water pressure (p_{wo}) and the apparent value of matrix suction (p_{co}) and B is a transport variable given by

$$B=\frac{k_{\mathrm{g}}A_{\mathrm{s}}}{2\eta_{\mathrm{g}}L_{\mathrm{s}}} \qquad (8)$$

where k_{g} is the effective gas permeability, A_{s} is the cross-sectional area, η_{g} is the viscosity of the gas and L_{s} the length of the specimen. The solution to the governing differential equation during the shut-in stage (i.e. when the injection pump is set to zero flow rate) gives:

$$p_{\mathrm{gi}}=p_{\mathrm{go}}\left[\frac{(p_{\mathrm{gi0}}+p_{\mathrm{go}})\exp(Ht)+(p_{\mathrm{gi0}}-p_{\mathrm{go}})}{(p_{\mathrm{gi0}}+p_{\mathrm{go}})\exp(Ht)-(p_{\mathrm{gi0}}-p_{\mathrm{go}})}\right] \qquad (9)$$

where p_{gi0} is the initial pressure of gas in the injection system, t is the elapsed time from stopping the pump and H is given by:

$$H=\frac{2\mathrm{B}\,\mathrm{p}_{\mathrm{go}}}{V_{\mathrm{gi0}}}$$

where V_{gi0} is the volume of gas at the start of the shut-in. Using this solution, a good fit to the data (Fig. 8b) was achieved with the following parameters: $A_{\mathrm{s}}=3.142\times10^{-4}\ \mathrm{m}^2$ (equates to the cross-sectional area of the central injection and back-pressure filters); $k_{\mathrm{g}}=2.55\times10^{-21}\ \mathrm{m}^2$; and $p_{\mathrm{co}}=0.5\times10^{6}$ Pa. Note this value is 0.5×10^{6} Pa smaller than that quoted in Harrington *et al.* (2012*a*), which was incorrectly cited. Although these may not be exactly correct, this technique can be used to produce an estimate for the expected duration of the test stage. Assuming that the conditions and material properties remain constant (which is a significant assumption), Figure 8b suggests that stage 22 may take around 680 days to reach an asymptote.

To examine the impact of gas migration on the hydraulic permeability of the mudstone and potential self-sealing behaviour, a second hydraulic test was undertaken on test COx-1 (Fig. 9). Although difficulties were encountered in modelling the data, probably because of the effects of residual gas in the sample and testing system, the axial permeability was estimated to be $1.65\times10^{-21}\ \mathrm{m}^2$ with a specific storage value of $4.5\times10^{-5}\ \mathrm{m}^{-1}$. For comparison, the hydraulic test conducted prior to gas injection yielded good fits to the model with an axial permeability of $2.0\times10^{-21}\ \mathrm{m}^2$ and a specific storage of $5.4\times10^{-6}\ \mathrm{m}^{-1}$. As such, there appears to have been only a small change in permeability because of the migration of gas, but an order of magnitude increase in specific storage. As indicated earlier, this is probably the result of the effect of residual gas within the sample pore space, clearly demonstrating that gas has fully penetrated the fabric of the clay. This may also explain the length of the hydraulic transient, which is significantly longer after the injection of gas (Fig. 9).

To further examine the self-sealing capacity of the COx, a second gas injection test following a simplified pressure history was undertaken. Analysis of the data (presented in Harrington *et al.* 2014), provided clear evidence for the spatial and temporal evolution of dynamic and unstable gas pathways. However, a cross-plot of flux v. excess gas pressure at steady state (Fig. 10) indicates little change in behaviour between test cycles, suggesting that the hysteresis observed between ascending and descending flow rates has been significantly reduced by the re-injection of water. Under these conditions, this observation suggests that gas has little permanent impact on the structure and fabric of the clay.

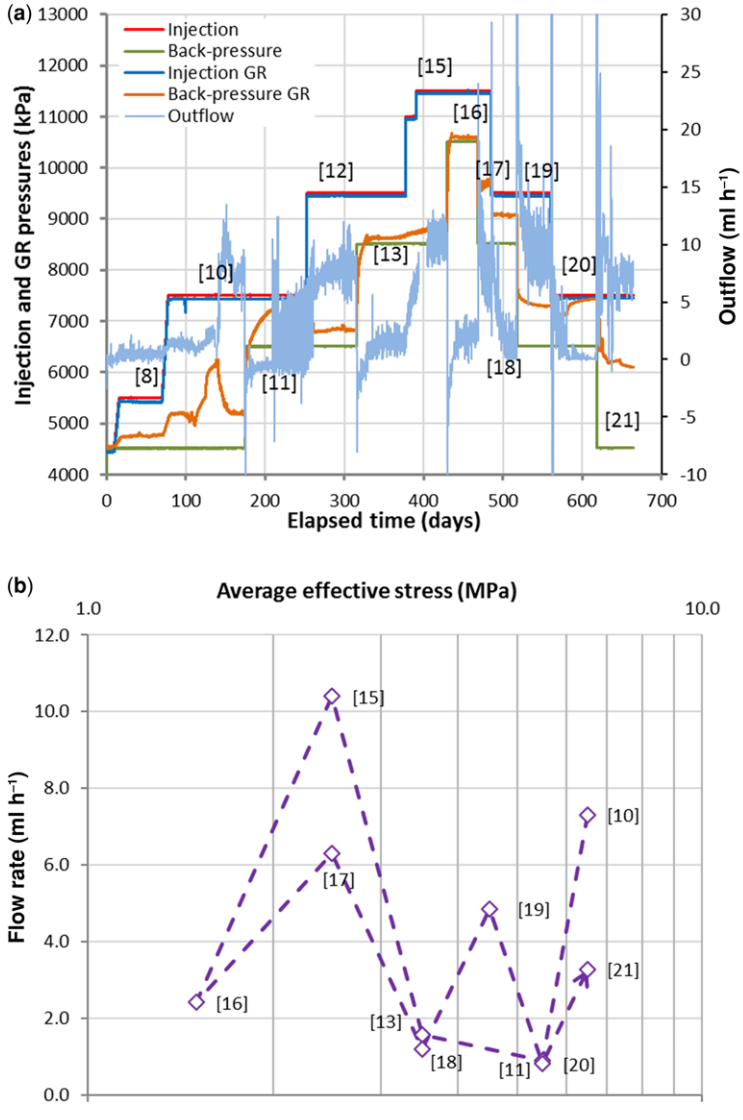

Fig. 7. Data from isotropic test COx-3. (**a**) injection, back-pressure, guard-ring (GR) pressures and outflow plotted against elapsed time. (**b**) steady state flow rate v. average effective stress.

Evidence of desaturation

Initial attempts to undertake a mass balance between the inflow and outflow during the drainage and imbibition cycles to estimate the change in saturation as a function of gas pressure gradient proved unsuccessful. Even taking a conservative approach to the calculation predicted unrealistically high gas saturations for relatively minor changes in excess gas pressure. This result directly contradicted the post-test measurements of sample desaturation, which uniformly showed post-test water saturation of 100%, i.e. no measureable desaturation. These results appear to confirm observations suggesting that dilatancy is a necessary component of advective gas flow through the COx. Analysis of volumetric strain data further supported this hypothesis, showing a clear correlation between gas permeability and bulk volume change of the sample.

Localization of flow

Following the completion of test COx-1, the sample was submerged in glycerol and gently heated to

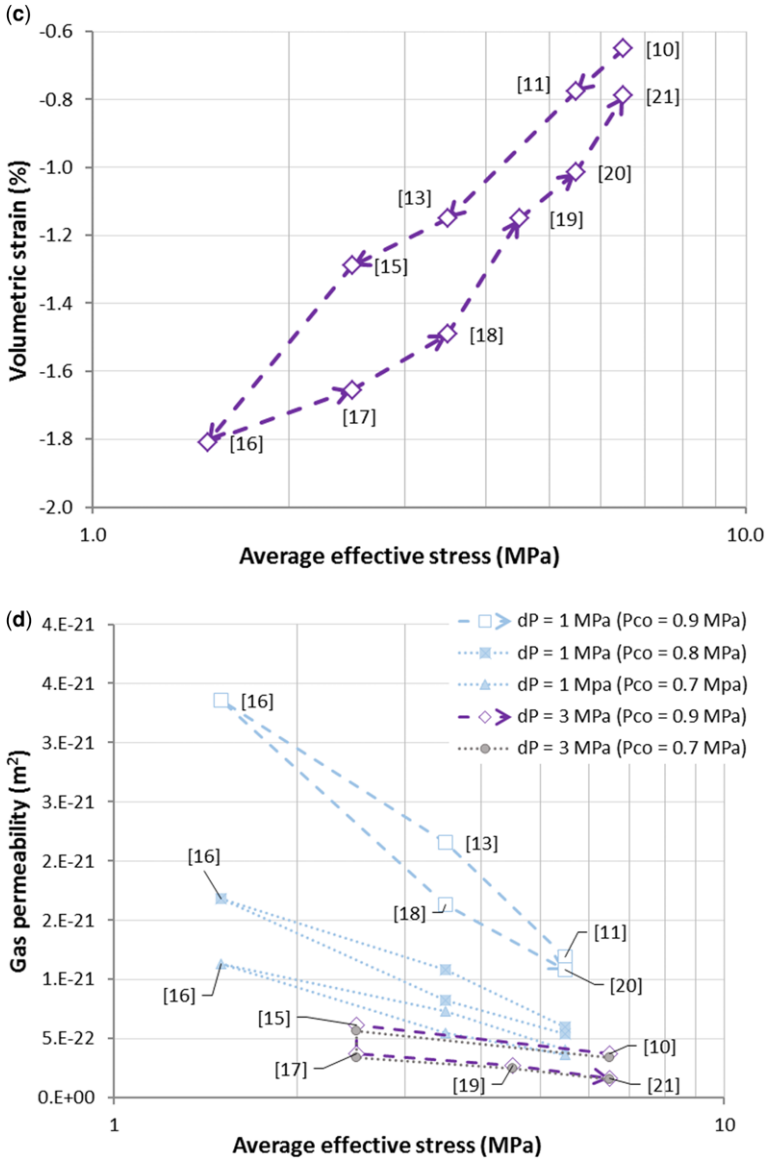

Fig. 7. (*Continued*) (**c**) cross-plot of volumetric strain versus average effective stress. (**d**) gas permeability for each test stage showing the sensitivity to p_{co} at low gas pressure gradients and indicating gas pressure gradient alone is not the only process governing flow.

promote the release of gas. Figure 11a, b show two images of gas discharged from the injection and back-pressure faces of the sample. Visual inspection clearly indicates a lower density of gas pathways on the injection face compared with that of the back-pressure end. Intuitively, this is to be expected and is symptomatic of an expanding network of pathways that fan out as they propagate through the core. It should be noted that a control sample of COx was also tested that had not undergone gas testing and no gas bubbles were seen to be expelled from the sample on heating.

To examine these zones in more detail, the sample was placed in a scanning electron microscope. Images taken from the face of the sample in a number of areas where bubbles were both absent and present appear to show the presence of localized microcracks (Fig. 11c, d, respectively). However,

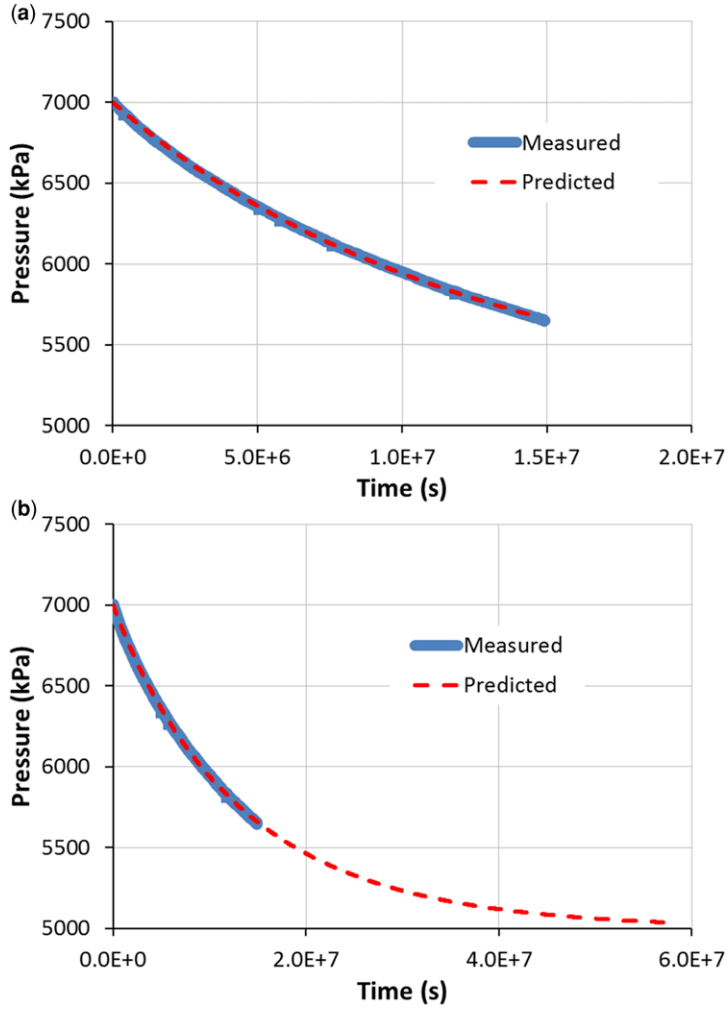

Fig. 8. (**a**) Shut-in response for test COx-1. The protracted nature of the shut-in response is a function of the initial gas volume and the non-linearity in the gas flow law. (**b**) a good numerical fit to the data can be obtained allowing a prediction of the capillary threshold pressure to be made.

although these features may relate to shrinkage artefacts during drying, the absence of cracks from sites where no gas was observed suggests that a correlation may exist. Although this method of observation is not fully quantitative, it indicates that gas flow is very localized within the clay. This observation supports the early results describing the evolution of guard-ring pressures and the time-dependent and non-uniform distribution of flow.

Modelling gas behaviour

Models of the gas injection experiment were constructed using the TOUGH2 porous medium multiphase flow code with the EOS3 equation of state module (Pruess *et al.* 1999). It was found that it was not possible to reproduce many of the important features of the data using these models (Fig. 12). In particular, the relationship between the onset of gas flow and the magnitude of subsequent flows could not be matched (Fig. 12c, d). Thus a model of the test on sample COx-1, which had an onset of flow at about 180 days as seen in the data, generated flow-rates that were typically a quarter of those seen. Conversely, a model that generated flow rates comparable with those measured had an onset of flow at about 40 days (Fig. 12).

Harrington *et al.* (2014) reported similar problems when modelling the gas injection test

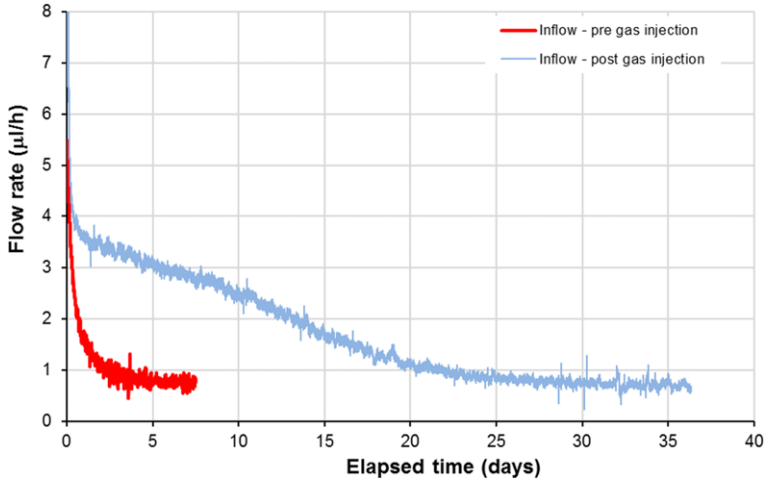

Fig. 9. Hydraulic inflow rate for sample COx-1 before and after gas injection. The length of the flow transient following gas injection may relate to the presence of residual gas.

performed on sample COx-2, again using TOUGH2. Setting the model parameters to match the observed response time of the injection guard-ring resulted in a predicted delay to the onset of gas outflow from the back-pressure filter until about 1300 days into the experiment, compared with the 600 days observed. Also, the gas flow rates were then about one-tenth of the rates seen in the test. Conversely, setting the parameters to give the onset of gas outflow at the time obtained in the test caused the model to show pressure changes at the injection guard-ring much earlier than seen in the test data. However, the gas outflow rates from this model were comparable with those obtained in the test. The short time delay between pressure responses at the injection and back-pressure guard-rings suggests that some form of direct pathway flow occurred rather than porous medium flow.

In modelling the data from test COx-1, Gerard *et al.* (2014) introduced a hydromechanical coupling and a hypothetical pre-existing fracture. By allowing fracture permeability and capillary entry pressure to vary with fluid pressure, Gerard *et al.* (2014) obtained a greatly improved fit to the data, highlighting the importance of the coupling between flow and mechanics.

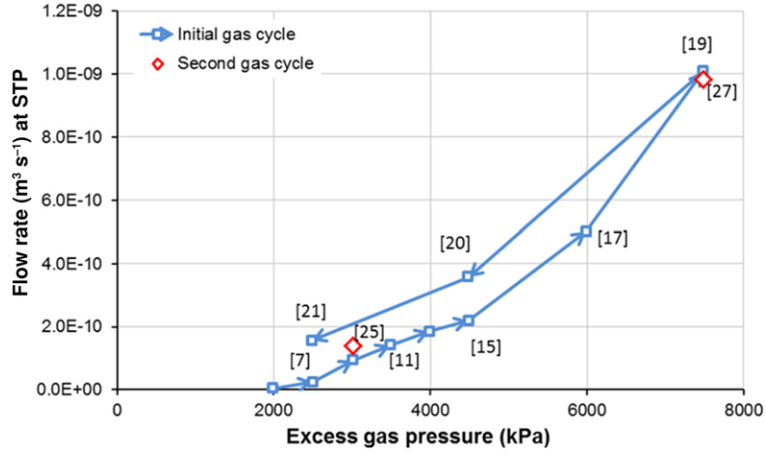

Fig. 10. Pressure and gas flow rate data from sample COx-1. Values in square brackets relate to stage numbers of the test described in Harrington *et al.* (2013).

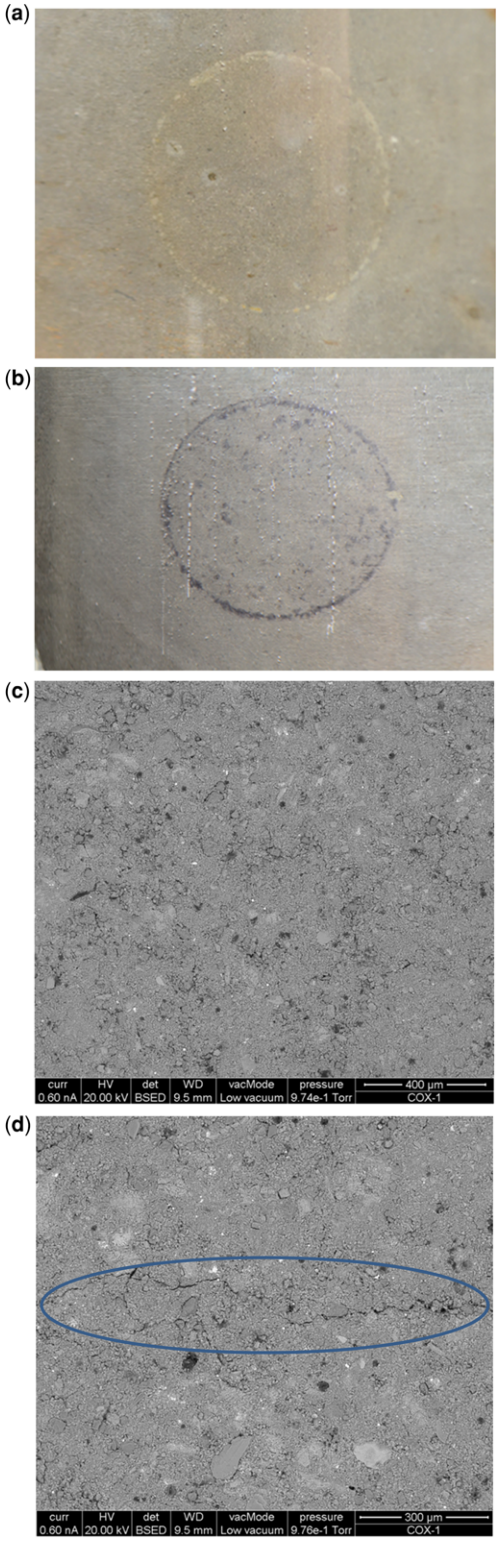

Gas flow through fractured COx

Fracture flow: hydraulic behaviour and stress sensitivity

To examine the impact of a fracture on the gas and hydraulic flow behaviour of COx, a sample was prepared, designated COx-4, containing a natural fracture (Fig. 2). Although this spanned the full length of the core, the sample retained some degree of cohesion between the fractured segments and remained 'intact', as shown in the photograph. As with all previous tests, the sample was subject to an initial *in situ* effective stress of 8 MPa. Following a period of re-saturation and equilibration, hydraulic testing was conducted (Fig. 13a).

To examine the sensitivity of the system to changes in stress, the confining pressure applied to the sample was reduced in a series of 1.5 MPa decrements (i.e. 9.0, 7.5, 6.0, 4.5, 3.0 and 1.5 MPa). Following this, the confining pressure was returned to the starting 9.0 MPa in two steps (4.5 and 9.0 MPa). Inspection of the data (Fig. 13a) suggests a subtle, continued reduction in permeability with time, which showed little apparent sensitivity to the change in confining pressure until 4.5 MPa confining pressure. Therefore, at stresses $<$4.5 MPa, enhanced flow was observed, suggesting that this stress level was sufficient to close the fracture. However, it should be noted that the value of permeability remained relatively high and was around one order of magnitude above that expected for intact COx (see Table 4).

It is worth noting that, for the majority of the test history, the flow in was similar to the flow out, suggesting that there was little net uptake of water and, in turn, a relatively low storage coefficient. This is clearly seen in Figure 13a, which shows that the majority of the water uptake following each stress change occurred within a short period immediately after the change in boundary stress. Thereafter, very little water appeared to migrate into the bulk rock mass of the sample. This further supports the idea that the fracture properties dominated the hydraulic behaviour of the sample, rather than the flow being distributed throughout the

Fig. 11. Gas discharge from sample COx-1 following submersion and gentle heating in a glycerol bath. The circular marks in images (a) and (b) are the imprints of the 20 mm diameter injection/back-pressure filters. (**a**) Injection face showing a relatively small number of bubble streams moving vertically upwards. (**b**) Back-pressure face with multiple bubble streams moving vertically upwards. (**c**) Image of one of the zones where no gas bubbles were observed. (**d**) Image of one of the zones showing microcracks (highlighted) in area of active gas discharge.

matrix. This is borne out in the observed hydraulic conductivity which, as noted earlier, is significantly higher than that for intact rock.

By tracking the net flow during this phase of testing (from day 43 onwards), it was possible to construct a soil mechanics plot of the void ratio against the average effective stress (commonly referred to as an e log P plot) (Fig. 13b). Inspection of the data clearly shows an increase in the sample volume as the effective stress decreased in a linear manner. Initially, this swelling-induced increase in porosity resulted in a small decrease in the bulk permeability, which then increased as the porosity increased and the confining stress on the fractured sample was reduced. As the confining pressure was increased at the end of the unloading cycle, the permeability followed an almost identical path to reach a final value of 2×10^{-20} m^2. By contrast, the void ratio followed a dissimilar path to that observed during unloading, suggesting that the porosity showed some degree of hysteresis. It is worth noting that the final void ratio at an effective stress of 7.75 MPa was almost identical to that seen at the same starting effective stress. Therefore, although hysteresis was seen during reloading, the final states were similar. Although the permeability paths observed during unloading and reloading were similar, a small difference between the start and final permeability values was noted. The sample was seen to dilate as the stress reduced, resulting in changes in the bulk modulus from 1200 to 120 MPa. These values are low, reflecting both the mode of measurement (see comments in the section on consolidation regarding the differences in Young's modulus) and the increase in compressibility induced by the reduction in stress.

Fracture flow: gas behaviour

Figure 14 shows the test history for the gas injection stage of test COx-4. Figure 14a shows that the test consisted of three pressure ramps. At the end of the second ramp the injection circuit pump was isolated from the system, which resulted in a decay in pressure at the injection filter. This shows that the gas entry pressure for the fractured sample had been exceeded. Figure 14b compares the predicted gas pressure from the ideal gas law with the injection pressure response and clearly shows that gas entry occurred at day 23.9 at an excess gas pressure of around 0.8 MPa. This value was low compared with the data for the intact material (Fig. 3), supporting the suggestion that sample 'damage' reduces the gas entry pressure. Figure 14c shows the flow data for the end of the second gas ramp. This clearly shows the onset of outflow from the sample, which signifies gas breakthrough. This occurred at an excess gas pressure of 3.2 MPa, although this will be dependent on the flow rate. A peak excess gas pressure of 6.0 MPa was achieved during the third gas injection stage. Following the end of pumping (gas shut-in), the pressure quickly decayed before entering a prolonged phase of slow pressure reduction. Although the asymptote was not fully realized, a 'shut-in' excess gas pressure of *c.* 1.5 MPa can be estimated. This is larger than the gas entry pressure for the sample, indicating that although gas can enter the fracture, it is unable to form an interconnected network of conductive pathways. It is also clear that gas entry and breakthrough occurred fairly early in the test history and that the fracture was able to sustain a high excess gas pressure of 6 MPa, which is one order of magnitude greater than the entry pressure. Following gas entry and breakthrough, the peak pressure was dependent on the permeability of the fracture. Therefore if the gas pressurization rate was slower, then the gas peak pressure would probably be less. Either way, the excess pressure of 6 MPa is still considerably lower than the effective stress of 8 MPa applied to the fracture.

Discussion

A series of long-duration laboratory tests was undertaken at the British Geological Survey to examine the fundamental mechanisms governing the migration of water and gas through the COx. These measurements demonstrated that, in the absence of pre-existing fractures, the movement of gas was associated with dilation of the clay fabric and a slow temporal evolution of the gas permeability within each specimen (Harrington *et al.* 2012*a*, 2013, 2014; Cuss & Harrington 2010, 2011, 2012; Cuss *et al.* 2014).

Spontaneous increases/decreases in the guard-ring pressures and downstream flux occurred throughout each test and are symptomatic of highly unstable dynamic pathways that opened and closed in an apparently random way. Such observations are difficult to reconcile with standard porous medium concepts.

The observed hysteresis between the drainage and imbibition responses is common (e.g. Harrington *et al.* 2009; Akbarabadi & Piri 2013) and signifies non-recoverability in the system. Post-test measurements of desaturation from tests COx-1 (Harrington *et al.* 2013) and SPP_COx-2 (Cuss *et al.* 2014) indicated no discernible displacement of the interstitial fluid from the original porosity. This, and the visual observations of localized degassing and accompanying microcrack formation, strongly suggest that the gas flow was through localized pathway dilation.

Although gas does not directly displace water in the creation of gas pathways, the development of

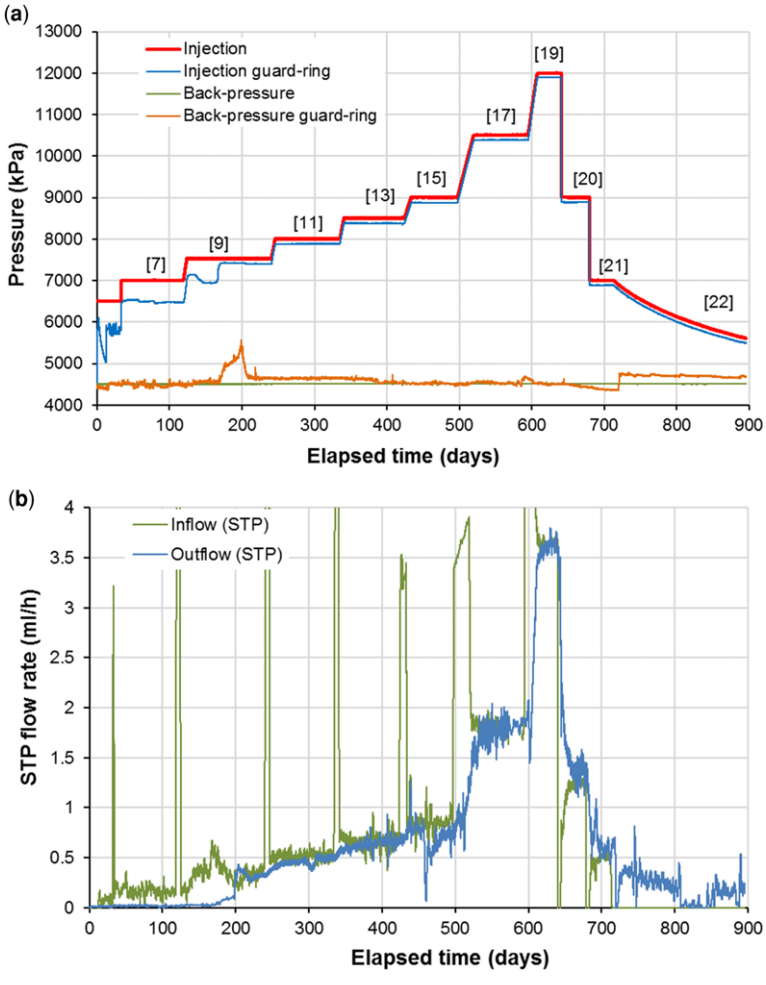

Fig. 12. Pressure (**a**) and flow rate (**b**) data collected during the gas injection test on sample COx-1 compared to TOUGH2 models that fit either.

gas porosity through dilation results in the localized deformation of the fabric adjacent to the flow paths. As such, this may mobilize very small volumes of water, which may also contribute to the hysteresis and lead to the time-dependent responses seen in the data. Whether or not the gas flow induces viscoelastic or viscoplastic responses remains unclear and further work is required to explore the coupling between stress, strain and gas flow.

The images of gas discharge from the injection and back-pressure faces of the core (Fig. 11b) suggest that a relatively small number of gas pathways are responsible for the transfer of gas across the sample. However, the geometry, size and spatial configuration of these features remains unclear because, at present, no technique is available with which to image the pathways in real time. In addition, the instability and ephemeral nature of these features mean that post-test imaging, including the techniques used in this paper, should be treated with caution, as some pathways may close on depressurization during decommissioning.

The inability of classic porous medium models to adequately represent the data is not surprising when we look at the response from the triaxial test SPP_COx-2 (Fig. 7b) prior to and after gas breakthrough and the clear hydromechanical coupling evident in test COx-3 (Fig. 8c, d). The data clearly show that gas flow is accompanied by a small, but well-defined, volume increase of the sample, which cannot be explained by compressibility calculations (Cuss *et al.* 2012). The data clearly exhibit time-dependent strain. As dilation increases, so does the volumetric discharge from the sample.

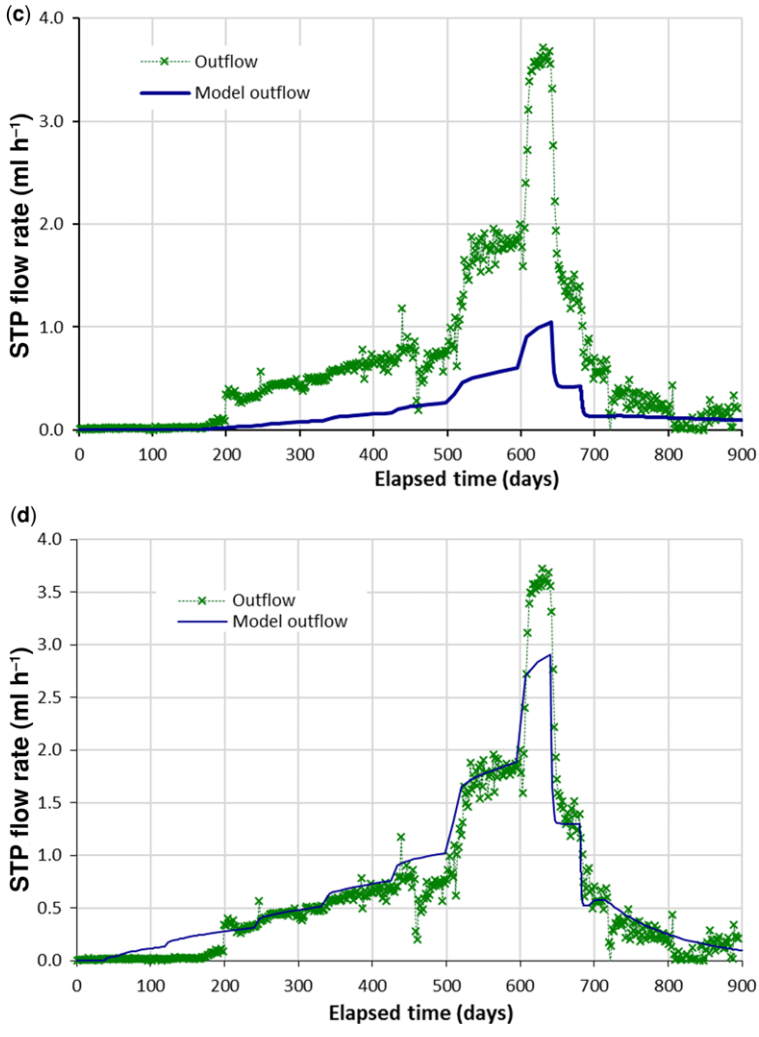

Fig. 12. (*Continued*) (**c**) outflow gas breakthrough time or (**d**) the outflow rates.

These data conclusively demonstrate that permeability is a dependent variable, integrally linked to the conductive pathways' aperture (manifest as volumetric strain in this test). It is interesting to note that, in the triaxial test (Fig. 6b), the observed increase in radial strain was non-uniform, suggesting localized flow within the sample. Further work is required to better understand the coupling between stress, strain, breakthrough and permeability.

However, the existence of time-dependent discrete pathway flow coupling gas pressure gradient, porewater pressure and stress has been well documented in pure clay systems (e.g. Horseman *et al.* 1996, 1999; Horseman & Harrington 1997; Harrington & Horseman 2003; Sathar *et al.* 2012). A similar coupling between gas flow and the development of dilatant pathways in natural plastic clays has also been proposed (e.g. Horseman & Harrington 1994; Ortiz *et al.* 1996; Sen *et al.* 1996; Harrington & Horseman 1999; Rodwell 2000; Harrington *et al.* 2009). Cuss *et al.* 2014 (which also contains observations from LAEGO-ENSG-Université de Lorraine, France) and Angeli *et al.* (2009) directly measured an increase in sample volume during gas flow. Similar observations were reported by Harrington *et al.* (2009, 2012*a*, 2014), who measured changes in the volume of the confining system during gas flow. Additional evidence for dilatant gas is provided by Harrington *et al.* (2012*b*), in which gold and titanium oxide nanoparticles were injected into an unlithified clay sample. Post-test scanning electron microscopy analysis found clay draped around

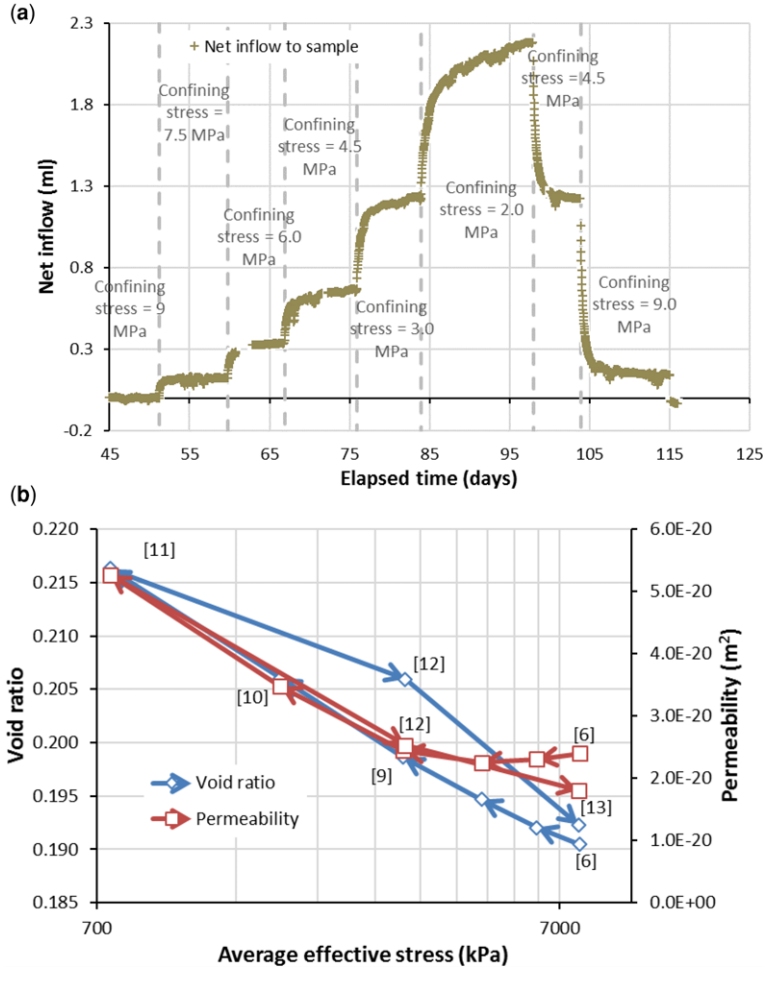

Fig. 13. (**a**) Net inflow of water as confining stress decreased and then increased for COx-4. (**b**) Void ratio and permeability against average effective stress for COx-4.

aggregates of gold particles, the latter only able to enter the clay if dilation of the fabric had occurred during gas flow.

In contrast with observations made on intact samples of COx, measurements performed on a naturally fractured sample (subject to hydrostatic stress) demonstrated that bulk permeability is controlled by the presence of the fracture. The unloading of the fracture resulted in a minimal change in permeability until a confining stress of 4.5 MPa, which suggests that this stress level is sufficient to close the fracture and/or prevent further damage to the sample. Reloading of the fracture resulted in a near-identical relationship of permeability with effective stress, although differences were noted towards the end-point of the path at the maximum effective stresses. As expected, the void ratio increased during unloading as the sample relaxed because the stress acting on the fracture reduced; at the same time, the bulk modulus reduced considerably. Hysteresis was observed during reloading, although the final void ratio was almost identical to the starting void ratio at a similar effective stress.

Gas flow through the fracture was, as expected, dominated by the presence of the fracture. A low excess gas pressure was sufficient to initiate gas flow. This observation adds weight to the hypothesis that tests conducted in samples damaged during sampling and/or preparation yield lower gas entry pressures as a result of their transport properties being dominated by microfractures (Fig. 3). By contrast, tests identified as intact, i.e. free from possible sample 'damage', can sustain excess gas pressures

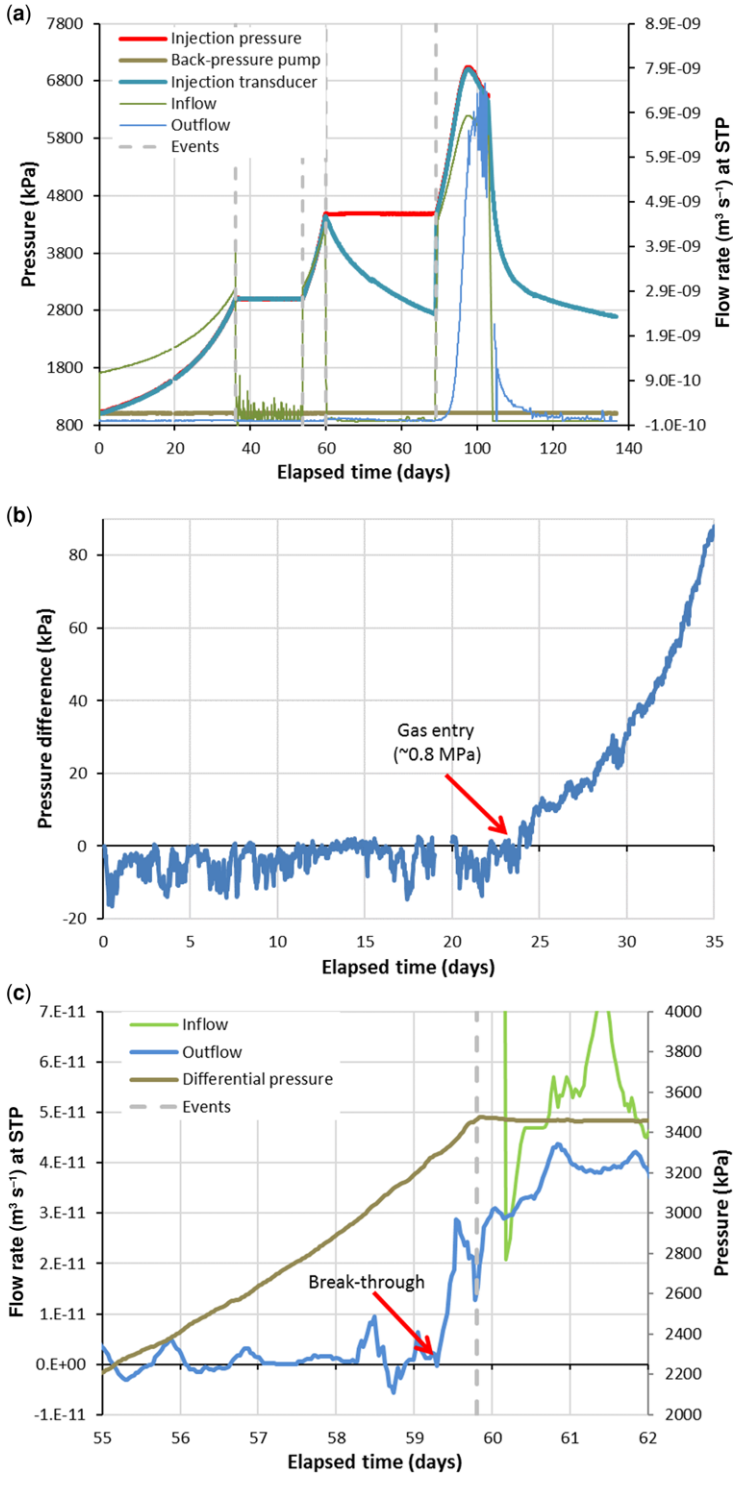

Fig. 14. Gas injection test conducted in a fractured sample (COx-4). (**a**) gas flow rates; (**b**) determining gas entry pressure; (**c**) determining gas breakthrough pressure.

close to the applied effective stress (Cuss *et al.* 2014). This tentatively suggests that samples which display gas entry/breakthrough pressures significantly lower than the effective stress may not reflect the properties of bulk intact rock.

It is clear that attempts to model these gas injection experiments in terms of porous media have been unable to reproduce significant aspects of the data because many features are indicative of the development of discrete flow pathways. As such, these results complement other studies that have shown the importance of the time-dependent, discrete pathway flow of gas in pure and natural plastic clays. Such behaviour should be considered in the future development of microstructural models aimed at describing gas advective flow in compact, saturated, clay-rich materials.

Conclusions

Based on a detailed analysis of laboratory data, it is our assertion that the advective movement of gas through initially intact, water-saturated COx can only occur through the development of pressure-induced dilatant pathways (i.e. the formation of pressure-induced microfissures). Dilation of these pathways, and therefore the surrounding fabric, occurs at gas pressures significantly below that of the minimum principal stress. Flow is through a local network of unstable pathways, the properties of which vary temporally and spatially within the mudstone. Gas flow appears to be highly localized, with visual observations suggesting a relatively small number of conductive pathways contributing to the flow of gas.

The coupling between gas flow and volumetric strain accounts for the time-dependent effects observed in this study, although further detailed work is required to better understand the coupling between stress, strain, breakthrough and permeability. As the gas flow is along pressure-induced preferential pathways, permeability is a dependent variable related to the number, width and aperture distributions of these features.

As expected, the hydraulic and gas transport properties in fractured samples are dominated by the properties of the fracture. Gas entry occurs at significantly lower pressures than those measured for intact rock. Microfissuring and engineering damage sustained during field sampling and specimen manufacture probably account for many of the low gas entry pressures observed by some researchers. Permeability of the fractured sample is stress-dependent, increasing significantly at confining stresses <4.5 MPa. Although the fractured sample exhibited minimal hydraulic hysteresis, gas testing of intact rock showed significant differences between the drainage and imbibition cycles, suggestive of potentially different controlling advective mechanisms. The data suggest that, although the act of injecting gas through intact COx has a significant effect on specific storage (through compressibility of the residual gas), the changes to permeability are minor.

The project was sponsored by the Agence Nationale pour la Gestion des Déchets Radioactifs (Andra) and the British Geological Survey (aligned to the Geosphere Containment Project). Experiments were conducted in the Transport Properties Research Laboratory, part of the Fluid Processes Research Group. The authors thank Dr David Noy for his work on numerical modelling of the data, Mr Antonio Milodowski for SEM imaging of the mudstone and Mr Humphrey Wallis and colleagues from the BGS Research & Design workshops who contributed to the design and manufactured the bespoke equipment used in this study. This paper is published with permission from the Executive Director of the British Geological Survey.

References

Akbarabadi, M. & Piri, M. 2013. Relative permeability hysteresis and capillary trapping characteristics of supercritical CO_2/brine systems: An experimental study at reservoir conditions. *Advances in Water Resources*, **52**, 190–206.

Altmann, S., Tournassat, C., Goutelard, F., Parneix, J.-C., Gimmi, T. & Maes, N. 2012. Diffusion driven transport in clayrock formations. *Applied Geochemistry*, **27**, 463–478.

Angeli, M., Soldal, M., Skurtveit, E. & Aker, E. 2009. Experimental percolation of supercritical CO_2 through a caprock. *Energy Procedia*, **1**, 3351–3358.

Cara, M., Cansi, Y. *et al.* 2015. SI-Hex: a new catalogue of instrumental seismicity for metropolitan France. *Bulletin de la Société Géologique de France*, **186**, 3–19.

Cuss, R.J. & Harrington, J.F. 2010. *Effect of Stress Field and Mechanical Deformation on Permeability and Fracture Self-Sealing: Progress Report on the Stress Path Permeameter Experiment Conducted on Callovo-Oxfordian Claystone*. British Geological Survey Commissioned Report, CR/10/151.

Cuss, R.J. & Harrington, J.F. 2011. *Update on Dilatancy Associated with Onset of Gas Flow in Callovo-Oxfordian Claystone: Progress Report on Test SPP_COx-2*. British Geological Survey Commissioned Report, CR/11/110.

Cuss, R.J. & Harrington, J.F. 2012. *Final Report of FORGE WP4.1.1: the Stress Path Permeameter Experiment Conducted on Callovo-Oxfordian Claystone*. British Geological Survey Commissioned Report, CR/12/140.

Cuss, R.J., Harrington, J.F., Graham, C.J., Sathar, S. & Milodowski, T. 2012. Observations of stable high-pressure differentials in clay-rich materials; implications for the concept of effective stress. *Mineralogical Magazine*, **76**, 3115–3129.

Cuss, R.J., Harrington, J., Giot, R. & Auvray, C. 2014. Experimental observations of mechanical dilation at the onset of gas flow in Callovo-Oxfordian claystone. *In*: Norris, S., Bruno, J. *et al.* (eds) *Clays in Natural and Engineered Barriers for Radioactive Waste Confinement*. Geological Society, London, Special Publications, **400**, 507–519, https://doi.org/10.1144/SP400.27

de Marsily, G. 1986. *Quantitative Hydrogeology for Engineers*. Academic Press, London.

Didier, M. 2012. *Étude du transfert réactif de l'hydrogène au sein de l'argilite*. Thèse de doctorat, Institut des Sciences de la Terre, Université de Grenoble 1.

Gaucher, E., Lerouge, C., Blanc, P. & Tournassat, C. 2007. *Caractérisation géochimique des forages PAC et nouvelles modélisations*. THERMOAR, BRGM/RP-54416-FR.

Gens, A., Vaunat, J., Garitte, B. & Wileveau, Y. 2007. In-situ behaviour of a stiff layered clay subject to thermal loading: observations and interpretation. *Geotechnique*, **57**, 207–228.

Gerard, P., Harrington, J., Charlier, R. & Collin, F. 2014. Modelling of localised gas preferential pathways in claystone. *International Journal of Rock Mechanics & Mining Sciences*, **67**, 104–114.

Harrington, J.F. & Horseman, S.T. 1999. Gas transport properties of clays and mudrocks. *In*: Aplin, A.C., Fleet, A.J. & Macquaker, J.H.S. (eds) *Muds and Mudstones: Physical and Fluid Flow Properties*. Geological Society, London, Special Publications, **158**, 107–124. https://doi.org/10.1144/GSL.SP.1999.158.01.09

Harrington, J.F. & Horseman, S.T. 2003. *Gas Migration in KBS-3 Buffer Bentonite: Sensitivity of Test Parameters to Experimental Boundary Conditions*. Report TR-03-02. Svensk Kärbränslehantering, Stockholm.

Harrington, J.F., Noy, D.J., Horseman, S.T., Birchall, J.D. & Chadwick, R.A. 2009. Laboratory study of gas and water flow in the Nordland Shale, Sleipner, North Sea. *In*: Grobe, M., Pashin, J.C. & Dodge, R.L. (eds) *Carbon Dioxide Sequestration in Geological Media – State of the Science*. AAPG Studies in Geology, **59**, 521–543.

Harrington, J.F., de la Vaissiere, R., Noy, D.J., Cuss, R.J. & Talandier, J. 2012*a*. Gas flow in Callovo-Oxfordian Clay (COx): Results from laboratory and field-scale measurements. *Mineralogical Magazine*, **76**, 3303–3318.

Harrington, J.F., Milodowski, A.E., Graham, C.C., Rushton, J.C. & Cuss, R.J. 2012*b*. Evidence for gas-induced pathways in clay using a nanoparticle injection technique. *Mineralogical Magazine*, **76**, 3327–3336.

Harrington, J.F., Noy, D.J. & Cuss, R.J. 2013. *Long-Term Gas Migration Experiments in Callovo-Oxfordian Claystone*. British Geological Survey, Technical Report, CR/13-088.

Harrington, J.F., Cuss, R.C., Noy, D.J. & Talandier, J. 2014. *Processes governing advective gas flow in the Callovo Oxfordian Claystone (COx)*. Fourth EAGE Shale Workshop, Porto, Spain, 6–9 April, 2014, https://doi.org/10.3997/2214-4609. 20140026

Horseman, S.T. & Harrington, J.F. 1994. *Migration of Repository Gases in an Overconsolidated Clay*. British Geological Survey, British Geological Survey, Technical Report, WE/94/7.

Horseman, S.T. & Harrington, J.F. 1997. *Study of Gas Migration in Mx80 Buffer Bentonite*. British Geological Survey, Technical Report, WE/97/7.

Horseman, S.T., Harrington, J.F. & Sellin, P. 1996. Gas migration in Mx80 buffer bentonite. *In*: *Symposium on the Scientific Basis for Nuclear Waste Management XX, Boston, MA, USA*. Materials Research Society, **465**, 1003–1010.

Horseman, S.T., Harrington, J.F. & Sellin, P. 1999. Gas migration in clay barriers. *In*: Pusch, R. & Yong, R.N. (eds) Microstructural Modelling of Natural and Artificially Prepared Clay Soils with Special Emphasis on the Use of Clays for Waste Isolation. *Engineering Geology*, **54**, 139–149.

Horseman, S.T., Harrington, J.F. & Sellin, P. 2004. Water and gas flow in Mx80 bentonite buffer clay. *In*: Oversby, V.M. & Werme, L.O. (eds) *Symposium on the Scientific Basis for Nuclear Waste Management XXVII (Kalmar)*, 15–19 June, 2003. Materials Research Society, **807**, 715–720.

Huyakorn, P.S. & Pinder, G.F. 1983. *Computational methods in subsurface flow*. Academic Press, New York.

INTERA Environmental Consultants 1983. *STAFAN: a Two-Dimensional Code for Fluid Flow and the Interaction of Fluid Pressure and Stress in Fractured Rock for Repository Performance Assessment*. Office of Nuclear Waste Isolation Report, ONWI 427.

Krooss, B.M. & Alles, S. 2008. *Experimental Studies on Caprock Sealing Efficiency and Gas Migration in Sedimentary Rocks*. Andra internal report.

Mjahad, S. 2012. *Étude de l'impact de la fissuration sur les propriétés de rétention d'eau et de transport de gaz des bétons, de l'argilite et des interfaces argilite/béton. Application au stockage des déchets radioactifs*. Thèse de l'université de Lille.

Ortiz, L., Volckaret, G. *et al.* 1996. MEGAS – Modelling and experiments on gas migration in repository host-rocks. *Proceedings of EU PEGASUS Meeting*, 14–15 June 1995, Rapolina-Terme, Italy. Nuclear Science and Technology Series, EUR 16746 EN. European Commission, Luxembourg, 127–147.

Ortiz, L., Volckaret, G. & Mallants, D. 2002. Gas generation and migration in Boom Clay, a potential host rock formation for nuclear waste storage. *Engineering Geology*, **64**, 287–296.

Pruess, K., Oldenburg, C. & Moridis, G. 1999. *TOUGH2 User's Guide, Version 2.0*. Lawrence Berkeley National Laboratory Report, LBNL-43134.

Robinet, J.C., Sardini, P., Siitari-Kauppi, M., Prêt, D. & Yven, B. 2015. Upscaling the porosity of the Caollovo-Oxfordian mudstone from the pore scale to the formation scale; insights from the 3H-PMMA autoradiography technique and SEM BSE imaging. *Sediment Geologyary*, **321**, 1–10.

Rodwell, W., Norris, S. *et al.* 2003. *A Thematic Network on Gas Issues in Safety Assessment of Deep Repositories for Radioactive Waste (GASNET). Final Report on the Treatment in Safety Assessments of Issues Arising from Gas Generation*. Nuclear Science and Technology Series, EUR 20620 EN. European Commission, Luxembourg.

Rodwell, W.R. (ed.) 2000. *Research into Gas Generation and Migration in Radioactive Waste Repository*

Systems (PROGRESS Project). Nuclear Science and Technology Series, EUR 19133 EN. European Commission, Luxembourg.

SATHAR, S., REEVES, H.J., CUSS, R.J. & HARRINGTON, H.J. 2012. Critical stress theory applied to repository concepts; the importance of stress tensor and stress history in fracture flow. *Mineralogical Magazine*, **76**, 3165–3177.

SEN, M.A., HORSEMAN, S.T. & HARRINGTON, J.F. 1996. *Further Studies on the Movement of Gas and Water in an Overconsolidated Clay: Contribution to MEGAS Phase 2 Report (PEGASUS Project)*. British Geological Survey, Technical Report, WE/96/8.

SONG, Y., DAVY, C.A. & TROADEC, D. 2016. Gas breakthrough pressure (GBP) through claystones: correlation with FIB/SEM imaging of the pore volume. *Oil and Gas Science and Technology–Revue d'IFP Energies nouvelles*, **71**, 51.

WEETJENS, E. & SILLEN, X. 2006. Gas generation & migration in the near field of a supercontainer-based disposal system for vitrified high-level radioactive waste. *Proceedings of the 11th International High-Level Radioactive Waste Management Conference (IHLRWM)*, 30 April–4 May 2006, Las Vegas, NV, USA, **30**, 1–8.

WIKRAMARATNA, R.S., GOODFIELD, M., RODWELL, W.R., NASH, P.J. & AGG, P.J. 1993. *A Preliminary Assessment of Gas Migration from the Copper/Steel Canister*. SKB Technical Report, TR93-31.

WILEVEAU, Y. & BERNIER, F. 2008. Similarities in the hydromechanical response of Callovo-Oxfordian clay and Boom Clay during gallery excavation. *Physics and Chemistry of the Earth*, **33**, S343–S349.

ZHANG, C.-L., ROTHFUCHS, T., SU, K. & HOTEIT, N. 2007. Experimental study of the thermo-hydro-mechanical behaviour of indurated clays. *Physics and Chemistry of the Earth*, **32**, 957–965.